SCIENCE CHINA
Technological Sciences

• Article •

December 2015 Vol.58 No.12: 2046–2051
doi: 10.1007/s11431-015-5935-8

# *In situ* study of the mechanical properties of airborne haze particles

DING MingShuai[1], HAN WeiZhong[1], LI Ju[1,2], MA Evan[1,3] & SHAN ZhiWei[1*]

[1] *Center for Advancing Materials Performance from the Nanoscale (CAMP-Nano) and Hysitron Applied Research Center in China (HARCC), State Key Laboratory for Mechanical Behavior of Materials, Xi'an Jiaotong University, Xi'an 710049, China;*
[2] *Department of Nuclear Science and Engineering and Department of Materials Science and Engineering, Massachusetts Institute of Technology, Massachusetts 02139, USA;*
[3] *Department of Materials Science and Engineering, Johns Hopkins University, Maryland 21218, USA*

Received July 24, 2015; accepted September 17, 2015; published online October 8, 2015

Particulate pollution has raised serious concerns regarding its potential impacts on human health in developing countries. However, much less attention has been paid to the threat of haze particles to machinery and industry. By employing a state-of-the-art *in situ* scanning electron microscope compression testing technique, we demonstrate that iron-rich and fly ash haze particles, which account for nearly 70% of the total micron-sized spherical haze particles, are strong enough to generate abrasive damage to most engineering alloys, and therefore can generate significant scratch damage to moving contacting surfaces in high precision machineries. Our finding calls for preventive measures to protect against haze related threat.

**haze particle, hardness, abrasive damage, precision industry**

**Citation:** Ding M S, Han W Z, Li J, et al. *In situ* study of the mechanical properties of airborne haze particles. Sci China Tech Sci, 2015, 58: 2046–2051, doi: 10.1007/s11431-015-5935-8

## 1 Introduction

Rapid industrialization and urbanization are often accompanied by air pollution. China, the world's largest developing country, is a striking example in past few years in this regard. Much of the country is currently suffering from intermittent severe air pollution [1–5]. The dense haze resulting from respirable suspended particles is now a common occurrence affecting large areas and population [1–5]. The sizes of these particles are usually in the range of tens of nanometers to a few micrometers, which is comparable to the abrasive particles used for chemo-mechanical polishing in the semiconductor industry. Therefore, in addition to the impacts of haze on visibility, human health and climate [6–9], it is likely that haze particles may reduce the service life of high-precision machine components through tribological wear, especially when under high-speed operation conditions and with the assistance of corrosive substances (i.e. $NO_x$ and $SO_2$) in the air [4].

A prerequisite for this hypothesis is that the haze particles are sufficiently hard to generate abrasive damage. However, to the best of our knowledge, there has been no quantitative test so far to probe the mechanical strength of individual haze particle. As a result, the potential hazard from haze particles to machinery remains speculative. Hence, there is a pressing need to probe into the mechanical properties of individual haze particle quantitatively. If indeed the measured hardness of the particle exceeds the wear criterion of engineering alloys, such particle should be able to scratch engineered surfaces, produce significant wear track and damage.

*Corresponding author (email: zwshan@mail.xjtu.edu.cn)

## 2 Methods

In this work, the airborne haze particles were collected on clean silicon substrates via natural deposition in a quiet area and then characterized inside a scanning electron microscope (SEM) and a dual beam focused ion beam (FIB).

### 2.1 Haze particle collection and characterization

Polished clean silicon wafer was put outside the window on the third floor (~10 m above the ground) of a quiet school building for 3–7 days to collect deposited particles during the haze season of 2014 in Xi'an, China. The building is located inside Xi'an Jiaotong University, which is at least 500 meters away from any main road with heavy traffic. After collection, the samples were directly characterized without additional processing. Morphology and chemical composition of the haze particles were analyzed utilizing a SEM (Hitachi SU6600) under the accelerating voltage of 15 kV. For the measurements of element silicon in haze particles, a silicon substrate covered by 2 μm thick copper film was used. Some spherical samples were cut using FIB with accelerating voltage of 30 kV and beam current of 93 pA for the cross-section observation. The category between $PM_{10}$ and $PM_{2.5}$ was roughly determined according to their physical size instead of aerodynamic diameter in this study.

### 2.2 *In situ* mechanical test and data analysis

*In situ* mechanical test was conducted using PI87 with a flat diamond tip inside the FIB (FEI Helios Nanolab 600) chamber under displacement rate controlled mode. The compression rate was programmed to be ~$6\times10^{-3}$ $s^{-1}$. The angle between the loading direction and the view direction was set to be 85° for better observation and video recording. The haze particles tested on the silicon substrate were identified by their chemical compositions, morphology, size and their relative locations to the substrate. The deformation processes were recorded at a scanning rate of 4 frames per second by a charge-coupled device camera. The accelerating voltage of the electron gun was set to be 10 kV during the test in order to reduce the potential beam damage. The contact pressure was defined as the applied force divided by the contact area between the particle and substrate assuming a perfect circular contact [10–12], and the compression ratio was defined as the compressive displacement ($u$) (after subtracting the contribution from the substrate) divided by the particle diameter ($D$) in our study. The $H_c$ was defined as the contact pressure at the point of yield for brittle particles or the peak contact pressure for ductile particles. The compression ratio at the point of $H_c$ is defined as critical compression ratio. The compression ratio programmed in the loading function was around 30% to 60%.

## 3 Results and discussion

It was found that both the size and morphology of the collected particles are very diverse (see Figure S1, Supporting Information). In order to simplify the data analysis without loss of generality, we have purposefully selected spherical haze particles as our research objects. A total of 146 spherical haze particles with their sizes ranging from 500 nm to 10 μm were analyzed. These all belong to the $PM_{10}$ (diameter ⩽ 10 micrometer) category, with 72% in the $PM_{2.5}$ (diameter ⩽ 2.5 micrometer) category as well and therefore are highly mobile in air and can remain suspended for long periods of time.

More than 10 different kinds of spherical particles were identified based on their main chemical composition (Figure S2 and Table S1). For the sake of simplicity, we classified them into four groups, i.e., fly ash, organic, iron-rich and others. As shown in Table S1, fly ash refers to the particles with aluminosilicate as their dominant composition; the main composition of organic particles is carbon and oxygen; the O/Fe atomic ratio of iron-rich particle is found to be in the range of 1.19 to 1.48. Occasionally, we also found that some pomegranate-like composite particulate with their seeds containing Ti, Pb, or Cr, as shown in Figure 1(d) and Figure S2. The number percentages of these four types of haze particles are 53.42% for fly ash, 19.18% for organic, 15.75% for iron-rich and 11.6% for others, respectively.

It is worth noting that the appearance of the particles can be very different. As shown in Figure 1, freshly collected fly ash particles usually have very smooth surface, but fine particles may adhere onto their surfaces as well (Figure 1(c)).

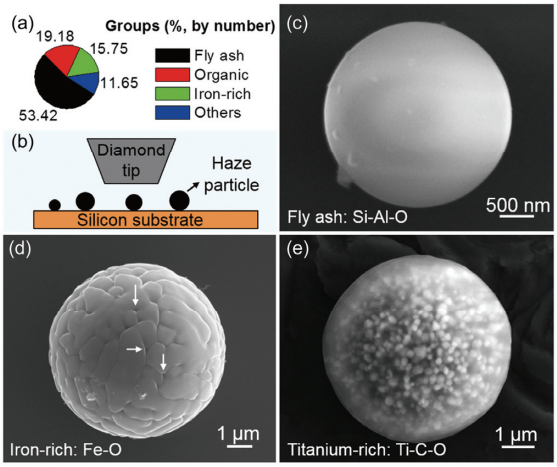


**Figure 1** (Color online) Proportion and appearance of spherical haze particles as well as the schematic experimental setup. (a) The fraction of four types of spherical particles based on the analysis of total 146 airborne haze particles with diameter ranging from 500 nm to 10 μm. (b) Schematic illustration of the setup for *in situ* SEM compression tests. (c) Fly ash, mainly aluminosilicate in composition. (d) Typical appearance of the brain-like iron-rich particle with miniature dongas distributed on its surface. (e) Pomegranate-like haze particle with numerous titanium oxides as seeds.

Organic particles mostly exhibit smooth surface (Figures S2(c), (e)). Interestingly, the appearance of iron-rich particles is size dependent. Large particles often have "valleys" or "dongas" on their surface (Figure 1(d)). Occasionally, small pit can be found at the triple junction of dongas, as marked with white arrows in Figure 1(d). These dongas will become sparse and even disappear with decreasing particle size (see Figure S3 for details). The most complex appearance comes from the organic-matrix composite particles. Under appropriate SEM imaging condition, they look like transparent pomegranates with numerous seeds. One typical example is shown in Figure 1(e). Analysis suggests that the internal "seeds" are titanium oxide. Even though their formation mechanism remains unclear, the composition and the appearance of the haze particles should carry hints of their formation mechanism and emission sources. Figure 1(b) is the schematic showing how these particles were tested mechanically. Even though organic particles are second behind the fly ash particles in the total number count, they are smaller (usually less than 1 μm) and much softer (see Movie S1) [13,14]. In this work, we focus on studying the mechanical behavior of the relatively harder spherical particles, as described below.

Fly ash particles can be classified into three main types depending on their mechanical response, i.e. brittle (e.g. Figure 2(a), black curve), less-brittle (e.g. Figure 2(a), red curve) and ductile (e.g. Figure 2(a), blue curve). Figure 2(a) shows the representative force vs. compression ratio (defined as $u/D$, where $u$ is the compression displacement and $D$ is the diameter of the tested particle) curves of these three types of fly ash particles. The corresponding diameters of the compressed particles in Figure 2(a) are 2320 nm (black), 2050 nm (red) and 2159 nm (blue), respectively. For the brittle fly ash particle, the compressive force increased steeply and linearly with increasing compression ratio. At the peak of the force, a large burst (Figure 2(a), black) occurred, where the sample fractured suddenly into two roughly equal parts and adhered to the flat indenter, as shown in Figure 2(b) (see Movie S2). The critical contact pressure ($H_c$, defined as the maximum force divided by the corresponding contact area upon the point of yield) is measured to be ~ 6.89 GPa. For the less-brittle fly ash particle, its stiffness (defined as the ratio between force and $u/D$) is obviously smaller than the brittle fly ash. In addition, the particle exhibited obvious yielding followed by some intermittent load drops (Figure 2(a), red curve and Movie S3). These load drops correspond to crack nucleation and propagation in the tested particle. Figure 2(c) is the top view SEM image of the less-brittle fly ash after the compression test. Compared to the completely through crack in brittle fly ash, the cracks (Figure 2(c), marked with white arrows) in less-brittle fly ash are much shorter in length. In contrast, the stiffness of the ductile fly ash particle is the smallest and its force vs. $u/D$ curve was quite smooth. Even though the residual strain is over 40%, no obvious yield can be identified from the loading curve (Figure 2(a), blue curve, Movie S4). After the test, the top view of the ductile fly ash still exhibits a round shape and no cracks can be detected, as shown in Figure 2(d). As displayed in Figure S4, the chemical compositions of fly ash particles do have obvious fluctuation. In addition to this difference in make-up, cross-sectional views revealed that 8 of the 12 fly ash particles examined had spherical inner cavities, which is similar to that of the fused ash bead [14]. One typical example is shown in Figure 2(e). The diverse mechanical responses of fly ash particles are most likely resulting from their different inner cavities (built-in flaws) as well as compositional variations (Figure S4).

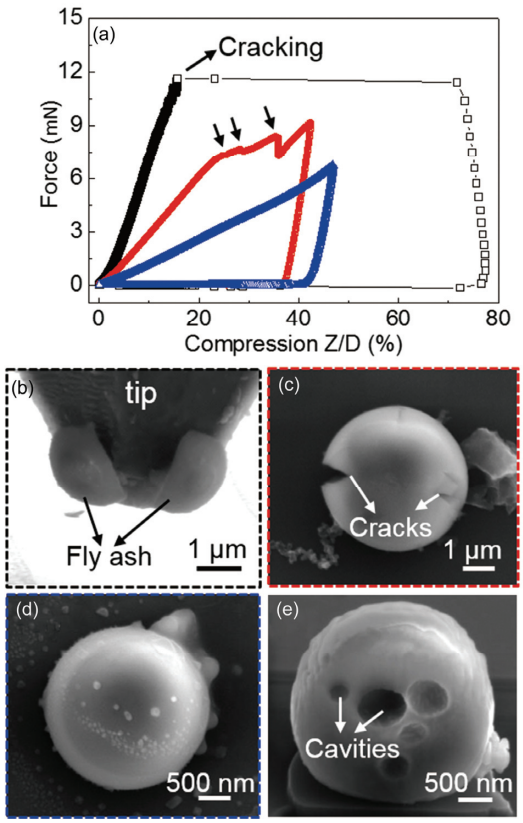


**Figure 2** (Color online) Compressive behavior of fly ash particles. (a) Representative mechanical curves of three types of fly ashes under compressive loading. Among the tested fly ashes, 2/11 were brittle (black curve), 6/11 were less-brittle (red curve) and 3/11 were ductile (blue curve). The black, red and blue curves correspond to the deformed particles in Figures 2(b)–(d), respectively. (b) Fragments of brittle fly ash adhered to the diamond tip after sudden failure as indicated by black arrows. (c) Postmortem top view of less-brittle fly ash. Cracks were found in the particle as marked with white arrows. (d) Top view of the round shaped ductile fly ash after deformation. No obvious cracks were identified. (e) Cross-section observation of a typical fly ash particle. Numerous nearly spherical cavities were found.

A total of 6 iron-rich particles were tested and all of them exhibited very high strength and brittle fracture. One typical example is shown in Figure 3 and Movie S5. The original diameter of this particle is 1386 nm. During the compression

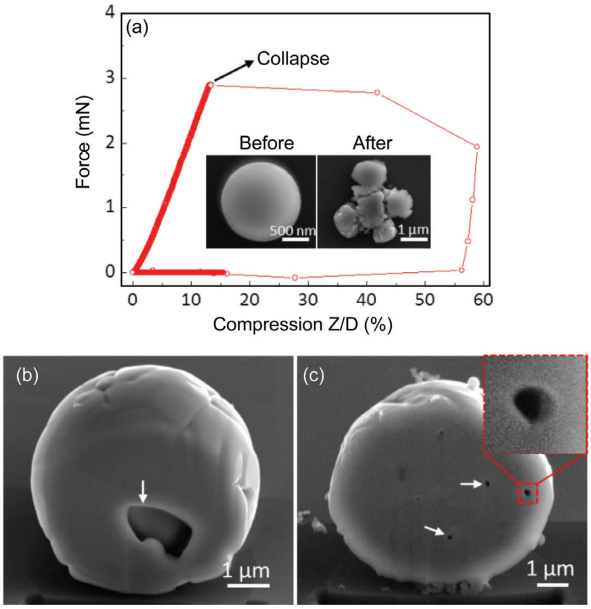


**Figure 3** (Color online) Compressive behavior of a typical iron-rich particle. (a) Typical force vs. compression ratio curve. The insets showed the top view of the particle before (left) and after (right) compression test. (b), (c) Cross-section examination of the iron-rich particles. Large and small sized cavities were indicated by arrows.

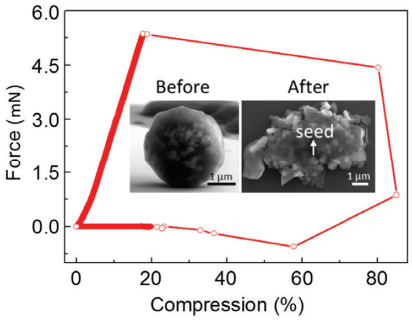


**Figure 4** (Color online) Compressive behavior of a pomegranate-like particle. Force vs. compression ratio curve of the particle. The insets displayed the morphologies before (left) and after (right) compression test.

test, force was observed to increase nearly linearly with increasing compression ratio to about 3 mN. Following this, a giant strain burst set in suddenly at the compression ratio of 13.6% (Figure 3(a)). The insets in Figure 3(a) are the SEM images of the iron-rich particles before (left) and after (right) the mechanical test. It can be seen that the particle was fractured into multiple fragments. The $H_c$ prior to the sudden fracture is measured to be ~ 9.76 GPa. On average, the $H_c$ of iron-rich particles is higher than that of fly ash particles (see Table S2). Cross-section examination demonstrated that 5 of 8 iron-rich particles contain irregular cavities inside (Figure 3(b) and (c)). The sizes of the cavities ranged from tens of nanometers to several micrometers. However, compared with the near spherical cavities observed in fly ash particles, the cavities in iron-rich particles is more irregular in geometry (Figure 3(b) and the inset of Figure 3(c)). Consequently, the corner of these cavities may serve as stress concentration sites during the compression test and lead to crack nucleation.

Pomegranate-like particles are complex and interesting in appearance and are different from all previously reported internal mixtures [15–17]. Their mechanical response is interesting as well. Our tests show that these pomegranate-like particles can yield at relative low stresses in a brittle manner. One typical example is shown in Figure 4 and Movie S6. This pomegranate-like particle mainly has titanium-rich seeds with original diameter of ~2.9 μm (left inset in Figure 4). Similar to the iron-rich particles, a giant strain burst set in after the load increased almost linearly to its peak value (Figure 4, red curve). However, the corresponding $H_c$ is only ~4.2 GPa. The top view SEM examination of the collapsed particle revealed that the residual morphology is like a broken concrete (right inset in Figure 4). This suggests that pomegranate-like particles may be formed through the mixture of metal-based seeds with carbon in a wet environment and dried out later.

Twenty-one spherical haze particles with diameters ranging from 940 nm to 6191 nm were mechanically tested in this work. As reported previously [10,18,19], the $H_c$ can be a key mechanical parameter to describe the mechanical strength of spherical particles. In this work, all the measured $H_c$ are plotted against their critical compression ratio in Figure 5(a). The iron-rich particles top all other haze particles in $H_c$. The majority of them reached a level of ~9 GPa with the maximum at ~11 GPa, which is comparable to the strength of silica slurry particles [11]. Fly ash particles rank the second, on average. It is worth noting that our mechanical tests were carried out inside a SEM. It has been reported that electron beam irradiation could induce softening in the ionic- and covalently-bonded samples [11,20,21]. If this effect is also present for iron-rich and fly ash particles, their $H_c$ without e-beam effect could be even higher.

As mentioned before, due to their tiny size and airborne nature, haze particles can easily get into moving parts in machinery, such as the bearing for high speed train, the gap between the cylinder and piston for car engine or turbine engine for airplane. However, in order to generate significant abrasive damage, the hardness of haze particles must be comparable or larger than the materials the parts are made of. According to the theory of contact mechanics [22], the compression of spherical particle is similar to an inverse indentation, and thus the $H_c$ of the haze particles can be seen roughly as their hardness. For comparison, Vickers hardness of frequently used metals and alloys in industry, such as steels in bearings, superalloys in aircraft, have been shown in Figure 5(a) (red color) [12,23–27]. It is obvious that the $H_c$ of iron-rich and fly ash particles are larger or at least comparable to the hardness of frequently used metals or alloys in industry (Figure 5(a), red color). If we define the hardness of a given material is $H_m$ and $K \equiv H_c/H_m$, according

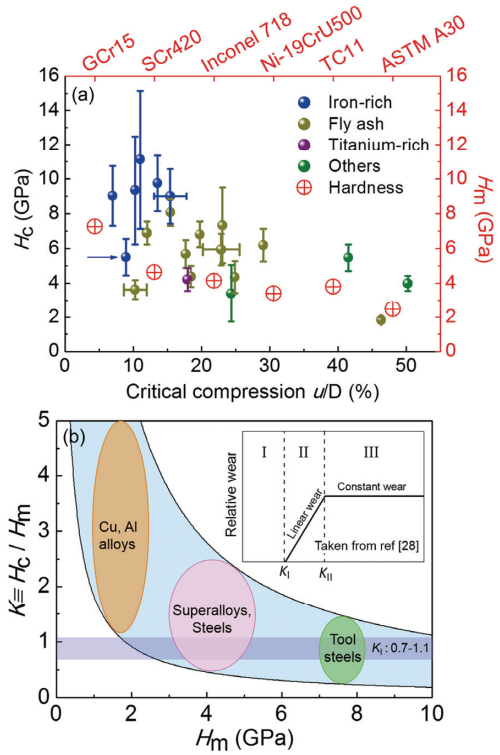


**Figure 5** (Color online) Critical criterions for generating abrasive damage. (a) Critical contact pressure ($H_c$) vs. critical compression ratio (left and bottom axis in black color) of 21 haze particles. The error bars came from the measuring error of the contact diameter between particles and substrate as well as the contribution from the substrate. For comparison, the Vickers hardness ($H_m$, right axis) of 6 frequently used metals (top axis) are also plotted in this figure with red color. (b) Relative hardness vs. $H_m$. The light blue area bounded by the $K_{max}$ and $K_{min}$ curves demonstrates the possible $K$ range of the haze particles shown in (a). The light purple region separates the non-wear zone (below) from the wear zone (above). The ellipses with different colors depict the $K$ range for several frequently used metals. The inset is the principle of abrasive damage taken from ref. [28].

to the principle of abrasive wear (as inserted in Figure 5(b)) [28], the two critical $K$ values, here denoted as $K_I$ and $K_{II}$, separate the relative wear into three zones: Non-wear zone I for $H_c/H_m \leqslant K_I$, linear wear zone II for $K_I < H_c/H_m < K_{II}$ and constant wear zone III for $H_c/H_m \geqslant K_{II}$. Therefore, in order to generate abrasive damage, $K$ must be larger than $K_I$. For the sake of clarity, by assuming that $H_m$ ranged from 0.4 GPa to 10 GPa, we plot the $K_{max}/K_{min}$ (defined as the maximum/minimum $H_c$ shown in Figure 5(a) divided by $H_m$) vs. $H_m$ curves in Figure 5(b), which bound the $K$ range of airborne particles, as highlighted by the light blue area. Numerous experiments indicated that the value of $K_I$ is among 0.7–1.1 [28], as marked by the light purple area in Figure 5(b). For comparison, the $K$ range of some frequently used metallic materials are also calculated and added in Figure 5(b) (as labeled in ellipses with different color). It can be seen that even for the tool steels with hardness up to 8 GPa, some hard haze particles are still able to cause serious wear since part of their $K$ is located in the wear zone (green ellipse). Therefore, if the haze particles float in, or are inhaled into, the moving contact surfaces in use, some of them will be strong/hard enough to generate scratch track and abrasive damage.

It is worth noting that for Vikers hardness, it has been demonstrated that measured hardness may increase with the decreasing indentation depth [29]. The underlying mechanism is that when the indentation depth is small (e.g. less than 500 nm), the indented volume has better chance to be free of defects and therefore yields ultrahigh hardness. However, once the indentation depth reaches a certain value, i.e. the indented volume is large enough, the Vickers hardness will become stable. In this work, the Vickers hardness we cited refers to the stable value. For the similar reason, free standing spherical particles may also exhibit size strengthening behavior, but only become significant when the diameter of the particles is small, say, in the sub-micrometer range [10]. In this work, the majority of the tested haze particles are larger than 1 micron meter. In addition, for the size range we have tested, no obvious size strengthening trend is observed. Therefore, size effect, even if existed, should not play a significant role in our discussion.

## 4 Conclusion

To summarize, we have characterized the diverse morphologies and chemical components of airborne haze particles and demonstrated the mechanical properties of the spherical ones by utilizing the *in situ* SEM mechanical compression method. We find that iron rich and fly ash particles, which account for nearly 70% of micrometer sized spherical haze particles, could withstand high contact pressure up to ~11 GPa. The critical criterions for generating abrasive damage as a result of haze particles were mapped in this work and the $K$ values for engineering materials are estimated to be partially located at the wear zone, revealing the significant threat of airborne haze particles to the industrial equipment. Considering the heavy particulate pollutions currently running rampant in developing countries, our findings suggest that appropriate preventive measures should be taken immediately to guard against the potential damage from haze, such as to assemble the precision parts in clean room, to seal the gap between sliding parts and to add special filter for air “breathing” engines. At the same time, more work should be continued to identify the sources of these particles and to understand their damage mechanism to specific industries.

### Supporting Information

The supporting information is available online at tech.scichina.com and www.springerlink.com. The supporting materials are published as submitted, without typesetting or editing. The responsibility for scientific accura-

cy and content remains entirely with the authors.

*This work was supported by the National Natural Science Foundation of China (Grant Nos. 51231005, 51471128 and 51321003), the National Basic Research Program of China ("973" Project) (Grant No. 2012CB619402), and the "111" Project of China (Grant No. B06025). W.Z.Han was supported by the Youth Thousand Talents Plan and the Young Talent Support Plan of XJTU. J.L. acknowledges support by the NSF DMR-1120901 and DMR-1410636.*

1 Seinfeld J H. Airpollution: A half century of progress. Am Inst Chem Eng J, 2004, 50: 1096–1108
2 Zhang Q, He K, Huo H. Cleaning China's air. Nature, 2012, 484: 161–162
3 WHO. Ambient (outdoor) air pollution in cities database 2014, http://www.who.int/phe/health_topics/outdoorair/databases/cities/en/, 2014
4 Guo S, Hu M, Zamora M L, et al. Elucidating severe urban haze formation in China. Proc Natl Acad Sci USA, 2014, 111: 17373–17378
5 Huang R J, Zhang Y L, Bozzetti C, et al. High secondary aerosol contribution to particulate pollution during haze events in China. Nature, 2014, 514: 218–222
6 Watson J G, Visibility J. Science and regulation. Air Waste Manage Assoc, 2012, 52: 628–713
7 Nel A. Air pollution-related illness: Effects of particles. Science, 2005, 308: 804–806
8 Chen R J, Zhao Z H, Kan H D. Heavy smog and hospital visits in Beijing, China. Am J Respir Crit Care Med, 2013, 188: 1170–1171
9 Wang Y, Zhang R Y, Saravanan R. Asian pollution climatically modulates mid-latitude cyclones following hierarchical modelling and observational analysis. Nat Commun, 2014, 5: 3098
10 Han W Z, Huang L, Ogata S, et al. From smaller is stronger to size-independent strength plateau towards measuring the ideal strength of iron. Adv Mater, 2015, 27: 3385–3390
11 Zheng K, Wang C C, Cheng Y Q, et al. Electron-beam-assisted superplastic shaping of nanoscale amorphous silica. Nat Commun, 2010, 1: 24
12 Shan Z W, Adesso G, Cabot A, et al. Ultra high stress and strain in hierarchically structured hollow nanoparticles. Nat Mater, 2008, 7: 947–952
13 Adachi K, Buseck P R. Internally mixed soot, sulfates, and organic matter in aerosol particles from Mexico City. Atmos Chem Phys, 2008, 8: 6469–6481
14 Meyer P W. Spheroidal Beads from Boiler Slag and Fly Ash; Ash Library, University of Kentucky, Center for Applied Energy Research: Lexington, KY, 1999. http://www.flyash. info/1999/newprod/meyer2.pdf
15 Pósfai M, Gelencsér A, Simonics R, et al. Particles from biomass and biofuel burning. J Geophys Res Atmospheres, 2004, 109: D06213
16 Li W J, Shao L Y. Mixing and water-soluble characteristics of particulate organic compounds in individual urban aerosol particles. J Geophys Res, 2010, 115: D02301
17 Li W J, Wang T, Zhou S Z, et al. Microscopic observation of metal-containing particles from Chinese continental outflow observed from a non-industrial site. Environ Sci Technol, 2013, 47: 9124–9131
18 Valentini P, Gerberich W W, Dumitrica T. Phase-transition plasticity response in uniaxially compressed silicon nanospheres. Phys Rev Lett, 2007, 99: 175701
19 Chrobak D, Tymiak N, Beaber A, et al. From bulk to nanoparticles: Deconfining nanovolume signals a shift in material. Nat Nanotech, 2011, 6: 480–482
20 Zhu X F, Su J B, Wu Y, et al. Intriguing surface-extruded plastic flow of SiOx amorphous nanowire as a thermally induced by electron beam irradiation. Nanoscale, 2014, 6: 1499–1507
21 Zheng H, Liu Y, Mao S X, et al. Beam-assisted large elongation of *in situ* formed Li2O nanowires. Sci Rep, 2012, 2: 542
22 Johnson K L. Contact Mechanics. Cambridge: Cambridge University Press, 1984
23 Zhang P, Li S X, Zhang Z F. General relationship between strength and hardness. Mater Sci Eng A, 2011, 529: 62–73
24 Zhang J G, Sun D S, Shi H S, et al. Microstructure and continuous cooling transformation thermograms of spray formed GCr15 steel. Mater Sci Eng A, 2002, 326: 20–25
25 Osada T, Gu Y Y, Nagashima N, et al. Optimum microstructure combination for maximizing tensile strength in a polycrystalline superalloy with a two-phase structure. Acta Mater, 2013, 61: 1820–1829
26 Zhu Y Y, Li J, Tian X J, et al. Microstructure and mechanical properties of hybrid fabricated Ti-6.5Al-3.5Mo-1.5Zr-0.3Si titanium alloy by laser additive manufacturing. Mater Sci Eng A, 2014, 607: 427–434
27 Riahi A R, Alpas A T. Wear map for grey cast iron. Wear, 2003, 255: 401–409
28 Khruschov M M. Principles of abrasive wear. Wear, 1974, 28: 69–88
29 Nix W D, Gao H J. Indentation size effects in crystalline materials: A law for strain gradient plasticity. J Mech Phys Solids, 1998, 46: 411–425